ACS APPLIED ELECTRONIC MATERIALS

pubs.acs.org/acsaelm

Article

Spatially Controlled Generation and Probing of Random Telegraph Noise in Metal Nanocrystal Embedded HfO_2 Using Defect Nanospectroscopy

Alok Ranjan,* Francesco Maria Puglisi, Joel Molina-Reyes, Paolo Pavan, Sean J. O'Shea, Nagarajan Raghavan, and Kin Leong Pey

Cite This: *ACS Appl. Electron. Mater.* 2022, 4, 3909−3921

Read Online

ACCESS | Metrics & More | Article Recommendations | Supporting Information

ABSTRACT: Random telegraph noise (RTN) is often considered a nuisance or, more critically, a key reliability challenge for miniaturized semiconductor devices. However, this picture is gradually changing as recent works have shown emerging applications based on the inherent randomness of the RTN signals in state-of-the-art technologies, including true random number generator and IoT hardware security. Suitable material platforms and device architectures are now actively explored to bring these technologies from an embryonic stage to practical application. A key challenge is to devise material systems, which can be reliably used for the deterministic creation of localized defects to be used for RTN generation. Toward this goal, we have investigated RTN in Au nanocrystal (Au-NC) embedded HfO_2 stacks at the nanoscale by combining conduction atomic force microscopy defect spectroscopy and a statistical factorial hidden Markov model analysis. With a voltage applied across the stack, there is an enhanced asymmetric electric field surrounding the Au-NC. This in turn leads to the preferential generation of atomic defects in the HfO_2 near the Au-NC when voltage is applied to the stack to induce dielectric breakdown. Since RTN arises from various electrostatic interactions between closely spaced atomic defects, the Au-NC HfO_2 material system exhibits an intrinsic ability to generate RTN signals. Our results also highlight that the spatial confinement of multiple defects and the resulting electrostatic interactions between the defects provides a dynamic environment leading to many complex RTN patterns in addition to the presence of the standard two-level RTN signals. The insights obtained at the nanoscale are useful to optimize metal nanocrystal embedded high-κ stacks and circuits for on-demand generation of RTN for emerging random number applications.

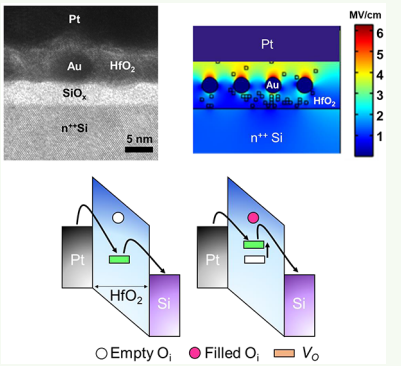

KEYWORDS: *conduction AFM, dielectric breakdown, metal nanocrystal, oxide defect, random telegraph noise*

1. INTRODUCTION

Random telegraph noise (RTN) is one of the general reliability problems for the ultrascaled semiconductor logic and memory devices.[1,2] In the context of transistors, RTN refers to the stochastic jump of the leakage current or threshold voltage between two or more discrete levels. For example, RTN often results in the temporal shift of the threshold voltage of a transistor, and in typical conditions, it could even lead to an erroneous read out of a memory state in emerging solid state memory, including resistive memory.[3,4] For the latter case, RTN effects are pervasive, especially for neuromorphic applications where the memory states are closely spaced and thus noise tolerance is low,[5] limiting the number of discrete states that can be reliably achieved. Interestingly, recent works have shown that the inherent randomness of RTN could be harnessed for many applications requiring on-demand random numbers. An emerging area is the security of the Internet of things (IoT) networks and devices which traditionally rely on the software and memory hungry chips for hardware verification resulting in hardware latency. A more robust and efficient means of implementing IoT security is the use of physical unclonable functions (PUF), which is a hardware circuit based on the inherent randomness in materials or manufactured semiconductor devices.[6] Another related application is true random number generators (TRNGs), where RTN is leveraged upon to produce the random unbiased bit stream.[7,8]

RTN in scaled electronic devices, including transistors and emerging memory technologies, can be traced back to the stochastic capture and emission of charge carriers at the atomic vacancies/defects in their dielectric materials.[9,10] For the widely used high-κ gate dielectric materials like HfO_2, the principal defects have been identified to be oxygen vacancies

Received: April 29, 2022
Accepted: July 7, 2022
Published: July 19, 2022

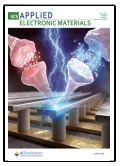

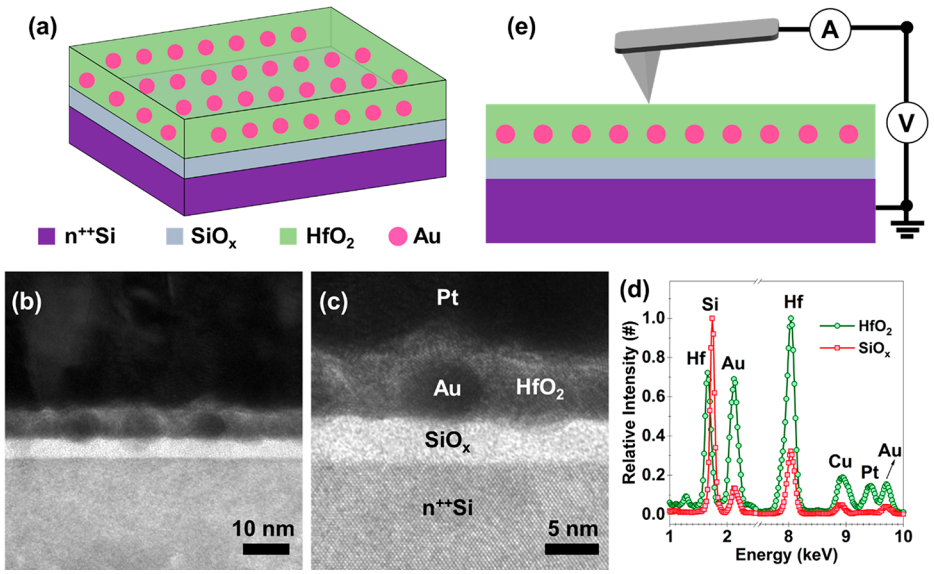

Figure 1. Metal nanocrystal embedded HfO_2 high-κ gate dielectric: (a) Schematic showing a 3D view of Au nanocrystal embedded in HfO_2. (b,c) TEM micrographs of the cross-section showing the growth of Au nanocrystals in 7 nm HfO_2. A 3.8−4.0 nm interfacial SiO_x layer is also formed during annealing (see sample preparation). The top Pt layer is deposited in the preparation of the TEM lamella. (d) Energy-dispersive X-ray spectroscopy (EDX) point spectra measured across HfO_2 and SiO_x layers showing the elemental composition. EDX spectra have been normalized to their respective counts. The elemental Cu trace in the EDX spectra is from the Cu TEM grid which is used to support the sample. (e) Schematic illustration showing a cross section of the Au embedded HfO_2/SiO_x sample and the electrical connections for CAFM measurements, in which the current and voltage across the tip−sample junction is measured.

(V_O) and oxygen interstitials (O_i).[11,12] Occasionally, an electron/hole is captured at a defect site during the charge transport, and it perturbs the local electrostatic environment around the defect.[13] The effect completely recovers when the trapped charge is emitted, and the original electrostatic environment is restored. In HfO_2 dielectrics, *ab initio* simulations and charge transport modeling have identified that positively charged oxygen vacancy (V_O^+) and neutral oxygen interstitials (O_i^0) defects are dominant.[14] While V_O^+, either isolated or clustered, have been shown to overwhelmingly contribute to the leakage current via trap assisted tunneling (TAT),[14] O_i^0 have been suggested to be responsible for low frequency noise and RTN.[10,15] Specifically, trapping/detrapping at the O_i^0 defect perturbs the potential on any nearby V_O^+ defect via Coulomb blockade, which in turn alters the TAT current flowing through the percolation path formed by the V_O^+. This mechanism also explains much of the variability of RTN over time, as the O_i^0 defects are relatively mobile and can diffuse into/out of the region where Coulomb interactions are significant around the V_O^+ defect.[16]

Primarily, three key parameters are often associated with RTN: (a) amplitude of the RTN (ΔI) − the difference between the high and the low current levels, (b) time to capture (τ_c) − the time spent in the high current level, and (c) time to emission (τ_e) − the time spent in the low current level. Using such parameters, earlier works have been mostly focused on understanding the impact of device scaling on the noise characteristics at the circuit level.[17] This approach has proven to be useful for the reliability qualification of a technology node. Experiments have considered measuring RTN of individual scaled devices, consisting of either transistor or capacitor test structures. The rationale of using this approach is that the number of defects can be significantly reduced as the device area is scaled, and this, in principle, can effectively allow probing RTN from a very small number of defects. However, a typical device size used in the reported literature varies between 100 nm to a few microns,[18] and consequently, 10−100 defects are present even in a 100 nm × 100 nm area device for a 10 nm thick, high-κ layer with a low defect density of 10^{17}−10^{18} cm^3.[14,19] The RTN measured is, in such cases, due to the cumulative effect of concurrent capture/emission events from multiple defect sites. An alternative experimental approach, used in this work, is conduction AFM (CAFM), which provides nanometer spatial resolutions to probe discrete defects.[20−22] CAFM has been developed to reliably measure low frequency noise in gate dielectric materials including SiO_2, HfO_2, and 2D h-BN.[23−26]

In addition to issues of electronic device reliability, new ideas are emerging about how to usefully apply RTN in technology. Recently reported works have shown that RTN has a clear potential use for TRNG[27,28] in security and cryptography applications, provided suitable materials for the reliable generation of RTN, preferably on demand, can be realized. As such, it is imperative to develop new dielectric material systems and understand the associated nanoscale dynamics that lead to RTN. Toward this goal, we study localized RTN signals by CAFM arising from Au nanocrystals (Au-NC) embedded in HfO_2. The nanocrystal embedded high-κ has an asymmetric field distribution under an applied voltage,[29] and hence, when the film is electrically stressed to soft breakdown (SBD), the defects giving rise to the RTN are localized in high field regions near the nanocrystal, providing a potential material platform to generate reliable, spatially localized defects for RTN based applications. By combining CAFM defect nanospectroscopy[23,24,26] and statistical analysis using the factorial hidden Markov model (FHMM),[30] our results highlight that a rich electrostatic interaction between defects in the HfO_2 provides a dynamic environment leading to many complex RTN patterns. Different patterns are readily observable within one experiment, making the nanocrystal

https://doi.org/10.1021/acsaelm.2c00559
ACS Appl. Electron. Mater. 2022, 4, 3909−3921

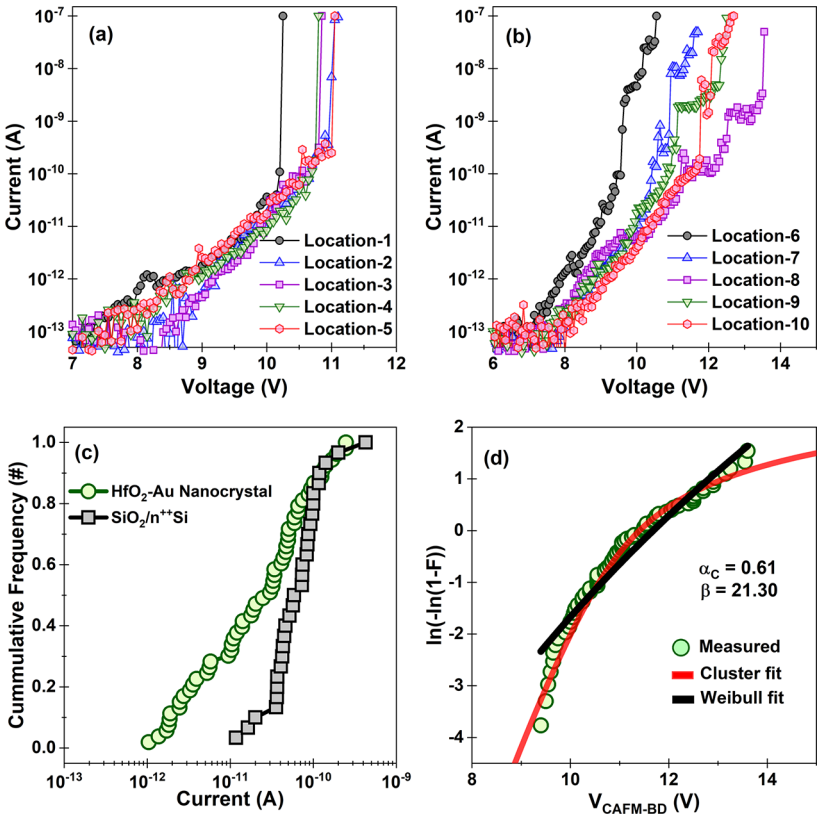

Figure 2. Electrical charge transport and statistical analysis of dielectric breakdown: (a) Representative $I-V$ characteristics measured across five test locations showing an abrupt jump in current at the instant of breakdown. (b) Representative $I-V$ curves measured at another five locations showing two discrete jumps in current prior to reaching the 100 nA current compliance. (c) Cumulative distribution plot of tunnel leakage current in HfO_2-Au nanocrystal/$n^{++}Si$ sample. Leakage current in a $SiO_2/n^{++}Si$ sample is also plotted for comparison. A total of 75 and 30 random locations are measured for Au-NC doped HfO_2 and SiO_2 samples, respectively. (d) Plot of the breakdown voltage ($V_{CAFM-BD}$) distributions in HfO_2-Au nanocrystal/$n^{++}Si$ sample on a Weibull scale along with cluster model fitting. Weibull model fitting is also shown for comparisons. $V_{CAFM-BD}$ is defined at the voltage at which leakage current reaches 100 nA. A total of 75 breakdown locations are used for the statistical analysis. It is important to note the HfO_2-Au nanocrystal layer also contains a SiO_x layer formed at the Si substrate interface during annealing.

embedded high-κ a good test structure for probing RTN phenomena in general. In comparison, previous works report that different RTN patterns are only infrequently detected within one test structure.[13,16]

2. RESULTS AND DISCUSSION

2.1. Test Structure and Physical and Chemical Characterization. The test sample consists of an Au-NC embedded HfO_2 gate dielectric stack on the $n^{++}Si$ substrate as schematically shown in Figure 1a. The details of sample preparation are in the Experimental Section. The $n^{++}Si$ substrate is purposely chosen rather than a bottom metal electrode to reduce surface roughness. Cross-sectional transmission electron microscope (TEM) analysis shows the HfO_2 layer thickness is ~7 nm, and the radius of Au-NCs varies between 2−3 nm, as shown in Figure 1b,c. The Au-NC are homogeneously distributed in the film (Figure S1). An additional 3.8−4.0 nm thick interfacial SiO_x layer between HfO_2 and the Si substrate is formed due to the thermal annealing step used for the nanocrystal formation. TEM analysis also shows that the Au-NCs are uniformly distributed across the sample and embedded in the high-κ layer. The spacing between nanocrystals varies between 5−7 nm, as shown in Figure 1c. The elemental composition of the prepared sample is confirmed using energy-dispersive X-ray spectroscopy (EDX), as shown in Figure 1d. Additionally, a high quality 3.3 nm thick SiO_2 sample is used as a control sample to compare the statistical variation of leakage current with the Au-NC embedded dielectric.

All the breakdown and RTN measurements are undertaken in an UHV-AFM working at a base pressure of ~2×10^{-10} Torr. The Au-NC embedded HfO_2 sample is used for CAFM experiments without further treatment, except for low-temperature annealing at 80 °C for 12 h in ultrahigh vacuum (UHV) to remove moisture present on the sample surface. A key consideration in our experiments is to establish a procedure which allows approximate control of the number of defects generated in the dielectric at the nanoscale. This is achieved by using CAFM to localize the breakdown region and controlling the maximum current flow allowed during the breakdown process. We implement this by integrating a Keithley 4200 semiconductor parameter analyzer externally to the AFM. A ramp voltage stress (RVS) is applied between the conducting tip and substrate, with a typical ramp rate of 0.25 V/s, and the maximum current flow is limited to 100 nA. RTN nanospectroscopy[23,26] is then carried out at these localized breakdown regions by applying a *fixed* voltage bias and recording the temporal variations in the current. As the Keithley 4200 analyzer has poor bandwidth for low current measurements in the pA−nA current range, for RTN data acquisition we use a different current amplifier (FEMTO DLPCA-200) with ~1 kHz bandwidth at 10^{11} V/A gain.[24] In

https://doi.org/10.1021/acsaelm.2c00559
ACS Appl. Electron. Mater. 2022, 4, 3909−3921

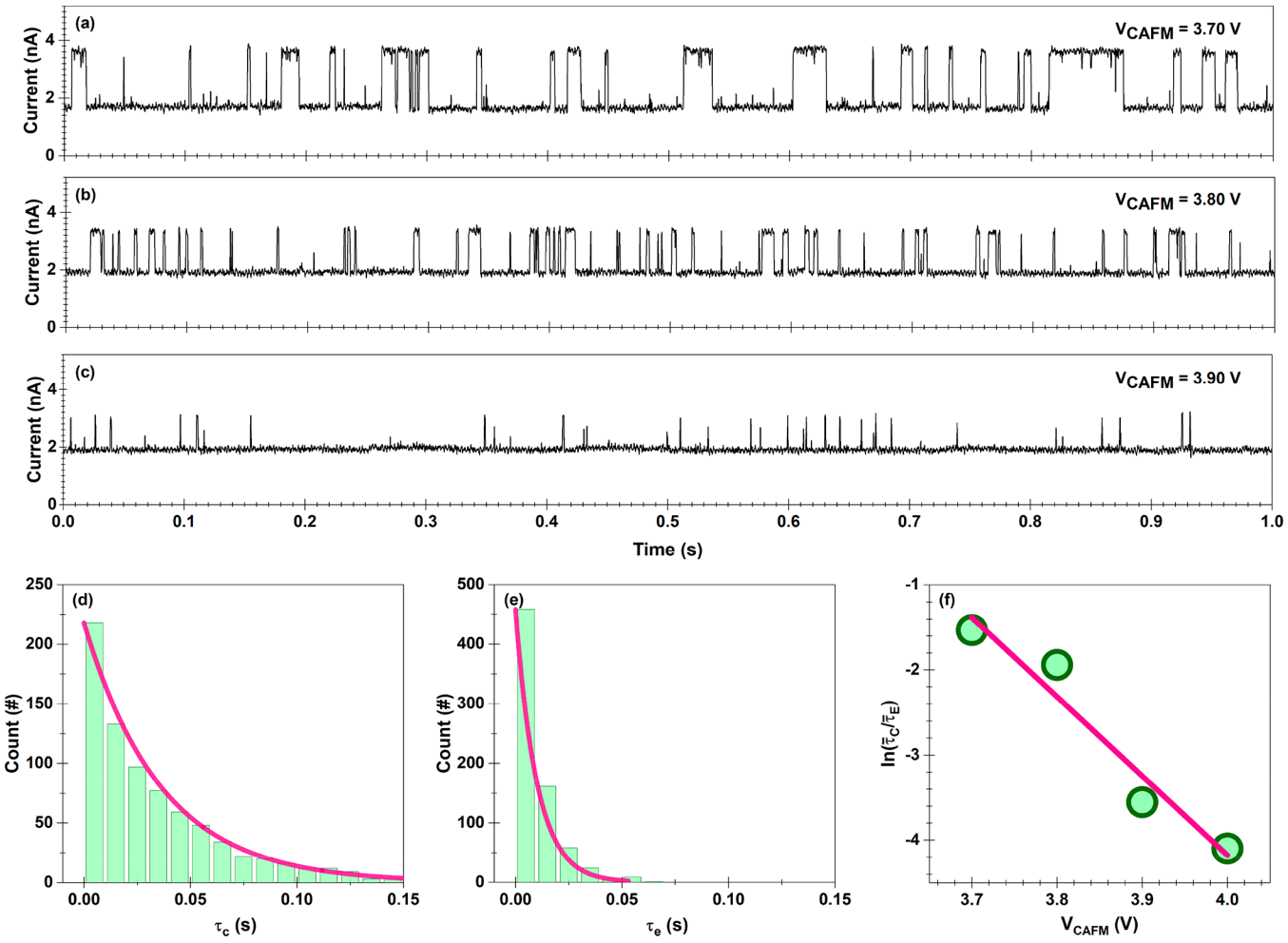

Figure 3. RTN defect nanospectroscopy: (a–c) A consistent two-level RTN measured after dielectric breakdown (I_{comp} = 100 nA) at bias of 3.70, 3.80, 3.90 V, respectively. Each RTN spectrum is acquired for a period of 60 s (see Figure S3 for complete spectra). The data plotted here shows only the initial one second period. (d,e) Histograms showing the distribution of capture time (τ_c) and emission time (τ_e) constants for the RTN data measured at 3.70 V. Both τ_c and τ_e follow an exponential distribution. (f) Plot of $\ln\left(\frac{\bar{\tau}_C}{\bar{\tau}_E}\right)$ and V_{CAFM} shows a negative slope which is used to estimate, to first order, the defect location (see text). $\bar{\tau}_C$ and $\bar{\tau}_E$ are average values for the capture and emission time, respectively.

all measurements, bias is applied to the tip, and the sample is electrically grounded.

2.2. Dielectric Breakdown and Defect Nanospectroscopy. The CAFM breakdown measurements are undertaken at ~75 randomly probed test locations, and the representative current voltage (I–V) characteristics are plotted in Figures 2a,b. Two different behaviors in the I–V curves are discernible. The majority (~85%) of the tested locations show a single abrupt jump in current at the instant of breakdown when the current reaches the current compliance of ~100 nA, as shown in Figure 2a. For the remaining 15% of tested locations, there is wider spread in the I–V traces, and at least two successive and distinct logarithmic jumps are observed in each I–V, as shown in Figure 2b. After the first RVS stress cycle, subsequent I–V curves at the same location indicate that the material under the tip has undergone soft breakdown (Figure S2). In general terms, electrical stressing creates defects in the oxide, and soft breakdown is characterized as a large increase in conductivity corresponding to the formation of a conducting path of defects linking the tip and substrate electrodes. In HfO_2, the conducting path principally consists of oxygen vacancy defects.[31,32]

The localized conductivity variations due to the presence of the NC can be obtained by comparing the distribution of the tunnel current across the sample. Specifically, we use the breakdown I–V curves to extract the tunnel current measured at 10.5 V for all the probed locations, as shown in Figure 2c. The tunnel current for the 3.3 nm $SiO_2/n^{++}Si$ sample, measured at 6.0 V, is also plotted for comparison. The variation in the measured tunnel current for Au-NC sample is spread over 2 orders of magnitude, which is an order of magnitude higher when compared with SiO_2. We should normally expect lower tunnel current variations for the much thicker HfO_2 film when compared with the thinner 3.3 nm SiO_2 *provided* the films are homogeneous, which is clearly not the case for the Au-NC sample. TEM micrographs, such as Figure 1b, show a stochastic distribution of the nanocrystal size and spacing, as well as variations in the thickness of both the SiO_2 and HfO_2 layers. These variations are reflected in the Au-NC breakdown data.

Following standard failure analysis approaches, we use the breakdown I–V curves to extract the breakdown voltage ($V_{CAFM\text{-}BD}$) and plot the data on a Weibull scale, as shown in Figure 2d. Here, $V_{CAFM\text{-}BD}$ is defined as the voltage at which

https://doi.org/10.1021/acsaelm.2c00559
ACS Appl. Electron. Mater. 2022, 4, 3909–3921

the leakage current reaches 100 nA. We note that $V_{CAFM\text{-}BD}$ is spread over a relatively large range, between 9.0 and 14.0 V, in line with the spread in the leakage current shown in Figure 2c. Figure 2d shows that $V_{CAFM\text{-}BD}$ in in the Au-NC sample does not follow a linear Weibull distribution, contrary to that observed in homogeneous HfO_2 and SiO_2.[33] An alternative defect clustering model, developed by Wu et al.,[34] has been shown to be successful in modeling the breakdown data in dielectrics having inhomogeneity, such as interface and line edge roughness.[35] The cumulative failure distribution (F_{CLUS}) for the clustering model is given by[34]

$$F_{CLUS} = 1 - \left(1 + \frac{1}{\alpha_C}\cdot\left(\frac{V_{CAFM\text{-}BD}}{\eta}\right)^{\beta}\right)^{-\alpha_C} \quad (1)$$

where α_C, β, and η are clustering factor, shape factor and mean breakdown voltage, respectively. The lower the value of α_C, the higher is the inhomogeneity in the dielectric, and as the value of α_C approaches infinity, the clustering model reduces to the Weibull model.[34] Analysis shows that the clustering model provides a better fit to the Au-NC data with α_C = 0.61, suggesting significant local inhomogeneity. There are several possible factors leading to this pronounced spatial inhomogeneity in the defect generation and thus breakdown voltage. As is apparent from Figure 1, the nanocrystal size and distribution, and the thickness of the dielectric layer near the NC vary. However, it is the consequence of these geometric variations that are more significant in that they result in a highly nonuniform field distribution under electrical stressing (see Section 2.5.1 and Figure 7b). Specifically, the electric field is enhanced at the periphery of Au-NC,[36] leading to greatly enhanced oxygen vacancy generation in these localized regions, as discussed more fully below with regards RTN creation. The nonuniform electric field, a consequence of incorporating the nanocrystals, is the primary factor leading to significant, localized breakdown inhomogeneity (i.e., low α_C). Other secondary factors could include the spatial variation of process-induced defects in both the high-κ and SiO_x layers, and slight variations in the contact area of the CAFM tip during experiments. It is to be noted that apart from the defect clustering model applied here, there are other statistical non-Weibullian models such as phase-type distributions[37,38] that could equally represent the nonlinear Weibit data observed in Figure 2d. Further investigations into the best statistical model for breakdown of NC-embedded dielectrics would be of potential relevance and will need to be accomplished.

2.3. Standard Two-Level RTN. We now discuss the RTN behavior of electrically created defects. Akin to prior breakdown measurements,[39] we use a stress and sense scheme; that is, defects are generated by RVS to relatively high voltage to cause SBD, and subsequently, at the same location, the RTN current fluctuations are measured at a much lower constant voltage bias. This procedure of creating RTN is similar to the forming operation of resistive random access memory (RRAM) devices.[40] Representative two-level RTN spectra measured at a bias of 3.7−3.9 V are shown in Figure 3a−c. Here, the spectra are plotted for one second (for brevity). The complete RTN spectra measured for 60 s at each bias is replotted in Figure S3. We observe that the RTN measured at 3.7 V is roughly equally distributed between the lower and the higher current levels. However, as the CAFM bias is increased up to 3.9 V, a noticeable decrease in time to capture (τ_c) is observed as the current stays in the higher current state for less time.

We use FHMM[30] for an efficient and reliable extraction of time constants for the relatively large RTN data sets shown in Figure S3. The distributions of both τ_c and τ_e for the RTN data measured at 3.7 V are plotted in Figures 3d,e, respectively, and they follow an exponential distribution. Similar trends are observed for all the other RTN data measured at a bias of 3.8−4.0 V, and the extracted values of $\overline{\tau}_C$, $\overline{\tau}_E$, and ΔI are shown in Table S1. The exponential distribution of time constants is akin to what has been observed previously in SiO_2 and high-κ gate dielectrics and is in-line with the expected behavior of RTN as predicted by all theoretical frameworks.[15,17]

The bias dependency of the RTN can be used to infer the physical location of the defect by supposing the defect to be isolated (at least in first approximation), that is, sufficiently far from other defects and/or charge centers. The relative position of the defect (Z_{eff}) in the dielectric as measured from the electrode from which the capture process occurs is estimated as[41]

$$Z_{eff} = V_T \cdot \frac{\partial\left(\ln\left(\frac{\overline{\tau}_C}{\overline{\tau}_E}\right)\right)}{\partial V_{CAFM}} \cdot \frac{EOT_{tot}}{EOT_{high\text{-}\kappa}} \cdot [\lambda + \mu(V_{CAFM})] \quad (2)$$

Here, V_T is the thermal voltage; V_{CAFM} is the sensing voltage; $\overline{\tau}_C$ and $\overline{\tau}_E$ are *average* capture and emission time constants, respectively; EOT_{tot} is the total equivalent oxide thickness; and $EOT_{high\text{-}\kappa}$ is the equivalent oxide thickness of the high-κ alone. These latter two terms are included to consider the effect of the SiO_x interfacial layer. However, the SiO_x layer typically also undergoes a breakdown (see Section 2.5.2 below), and in this case, the formula should not include the EOT correction; however, given that the value of the term is 1.08, there is little difference between the two situations. Of more importance is the relative distance from the electrode. If the SiO_x was not broken, Z_{eff} would be measured from the Si/SiO_x interface. In our experiments, we take Z_{eff} from the SiO_x/HfO_2 interface because the SiO_x is usually broken. The term in square parentheses is a correction term to the classical formula[41] that is included to take into account the effects of the structural relaxation accompanying the TAT process and the possible nonmonotonicity of the $\ln\left(\frac{\overline{\tau}_C}{\overline{\tau}_E}\right)$ vs V_{CAFM} trend. Typically, this correction term is ignored by setting λ = 1 and μ = 0. In our case, the experimentally observed $\ln\left(\frac{\overline{\tau}_C}{\overline{\tau}_E}\right)$ vs V_{CAFM} trend is largely monotonic, and therefore we set μ = 0, and to consider (to first order) the effects of structural relaxation[41] we set λ = −2. The plot of $\ln\left(\frac{\overline{\tau}_C}{\overline{\tau}_E}\right)$ and V_{CAFM} shows a monotonic slope of −9.28 ± 1.62 as shown in Figure 3f. This suggests that the defect causing RTN, in this case, is located in the HfO_2 layer approximately 3.36 ± 0.59 nm away from the SiO_x/HfO_2 interface. Although useful to obtain some indication of defect location, it must be highlighted that the analysis is approximate as the electronic effect of the Au-NC is not known.

Dynamic electrostatic rearrangements in the local atomic environment near the RTN defect appear as temporal perturbation of the RTN signal.[16,42] Often such perturbations are subtle and masked in the overall signal. For example, a noticeable change in the RTN pattern measured at 3.70 V in Figure S3 can be observed between 35−40 s. We find that

https://doi.org/10.1021/acsaelm.2c00559
ACS Appl. Electron. Mater. 2022, 4, 3909−3921

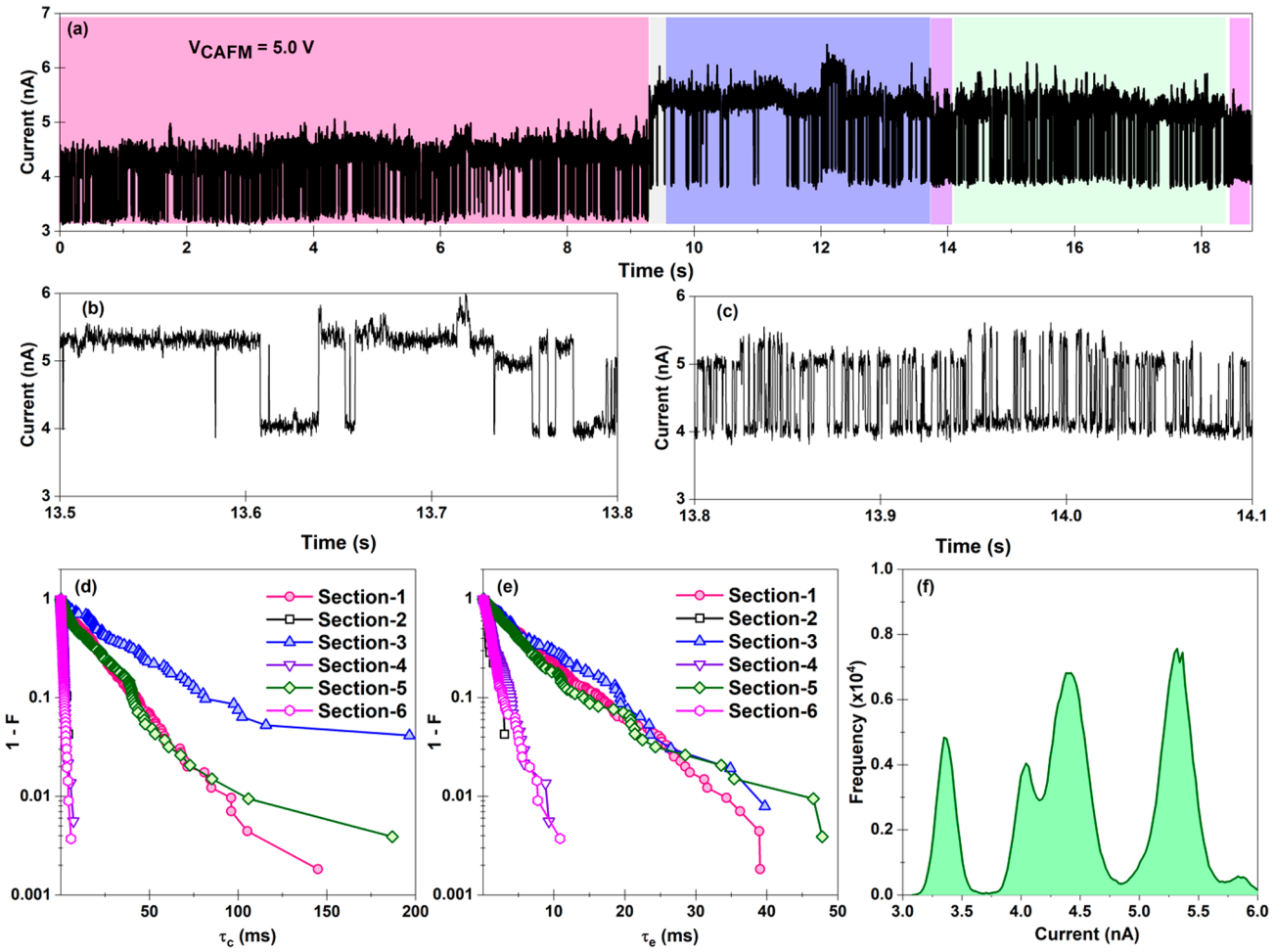

Figure 4. Mutant RTN showing variable characteristics: (a) RTN spectra measured after SBD at a bias of 5.0 V at a randomly chosen test location. There is an abrupt change in the RTN characteristics at t = 9.3 s. (b, c) Zoom-in view of the two representative sections of the RTN data in (a) showing the presence of both slower and faster current transitions. (d, e) Plot of the distribution of τ_c and τ_e for the six sections of the RTN spectra in (a) shows that all the six sections can be grouped in two categories: slower and faster current transitions. Sections 1, 3, 5 belong to the slow current fluctuations, while Sections 2, 4, 6 show faster transitions. (f) Histogram plot of the RTN in (a) showing the different current levels. Four current levels are distinguishable.

FHMM can serve as a useful tool to analyze such changes. The entire RTN data measured at 3.70 V is segmented into three subsections. Each of these is analyzed using FHMM, and the results are summarized in Table S2. It is found that ΔI is the same for Section 1 and Section 3, while it is smaller for Section 2, an effect that is also readily observed visually and, also in the histogram, as shown in Figure S4. However, a less obvious result revealed by the FHMM analysis is that the average capture time ($\overline{\tau}_C$) for Section 1 and Section 3 are identical (within the uncertainty that naturally exists[43] by considering only a finite number of samples per section—see Table S2), while in Section 2, the value of $\overline{\tau}_C$ is lower. These features are all consistent with the existence of some temporally localized electrostatic perturbation of the defect causing RTN during Section 2. This effect is sizable and alters the estimation of the capture time if the whole-time trace were taken as the sample data; an effect not readily observed in standard histogram distributions as in Figure 3d,e.

2.4. Other Types of Nonstationary RTN. In addition to the standard two-level RTN, we find that Au-NC embedded HfO_2 exhibits many types of nonstationary RTN signals. Following the nomenclature of Puglisi et al.,[16] these include the following: multilevel RTN, the superposition of several individual two-level signals; mutant RTN, a two-level RTN which changes statistics (τ values or ΔI) before returning to the original RTN signal; and temporary RTN, a 2 level RTN appearing/disappearing over time. Another form, called anomalous RTN, also manifests as an appearing/disappearing RTN signal but differs from temporary RTN in that it represents a *correlated* interaction between a two-level RTN defect and other RTN fluctuations.[16] For simplicity, in this work, we make no distinction between anomalous and temporary RTN. We present analysis for several of these nonstationary RTN in this section. We highlight that although such nonstationary RTN have been reported earlier in high-κ based NVM devices,[42] it is the first time, to our knowledge, that a systematic analysis of all such nonstationary and complex RTN patterns as detected on a single material stack is reported.

2.4.1. Mutant RTN. First, we present an example in Figure 4 where the RTN behavior changes with time. At a first glance, the RTN spectrum in Figure 4a appears to be a standard two-level RTN, except that there is an abrupt increase in the overall current level at t = 9.3 s. This is possibly due to either creation of a new TAT defect, increasing the overall current, or a spatial rearrangement of one or more defect(s). Careful inspection shows that the overall RTN spectrum is composed of a

https://doi.org/10.1021/acsaelm.2c00559
ACS Appl. Electron. Mater. 2022, 4, 3909−3921

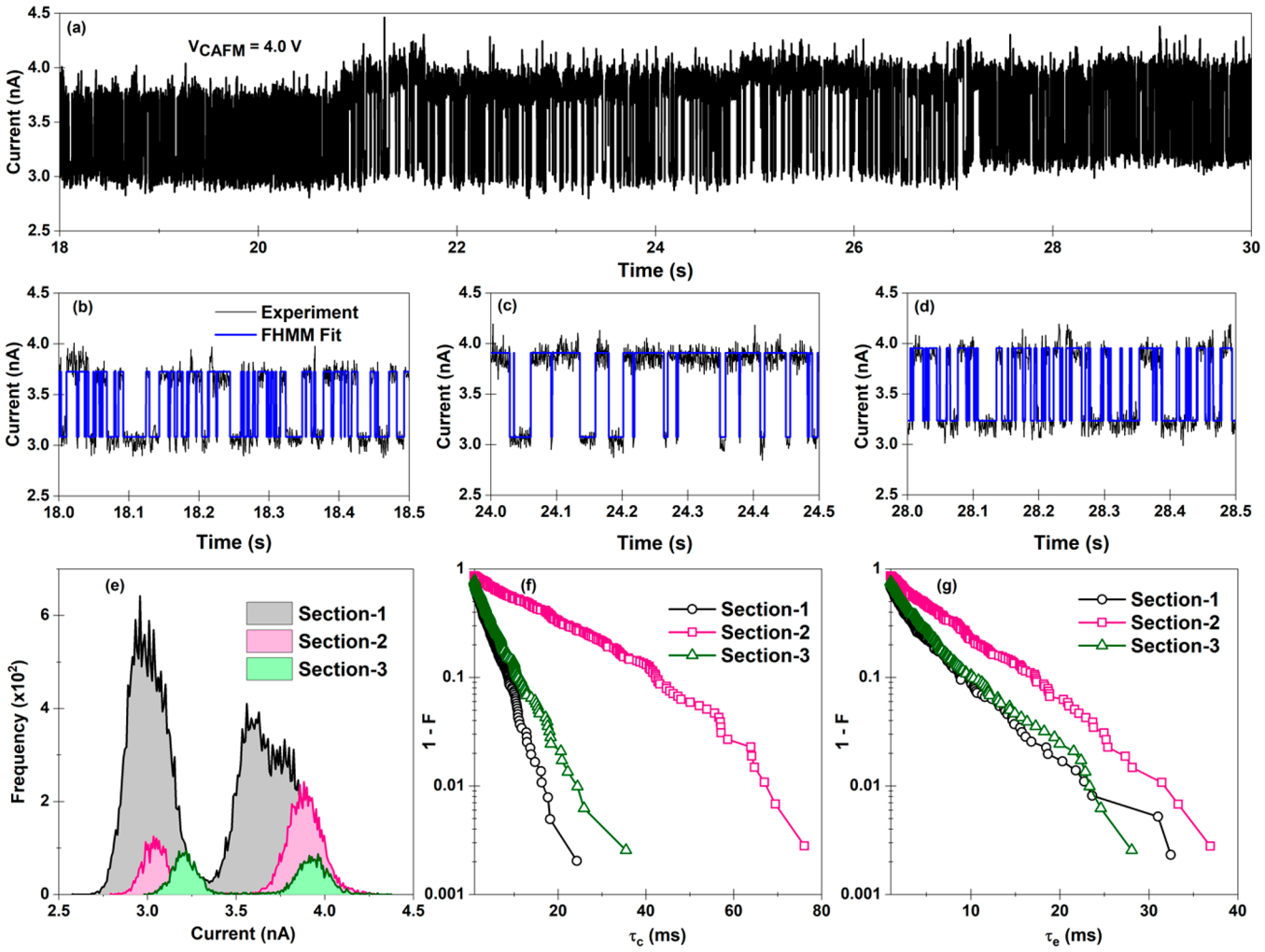

Figure 5. Mutant RTN showing variation of time constants: (a) RTN measured after SBD at a bias of 4 V at a randomly probed test location. Only a section of the RTN spectra between 18−30 s is shown to highlight the slower and faster current transitions present. The complete RTN spectra is plotted in Figure S5. (b−d) Zoomed-in view of the portions of the three sections of the RTN in (a) showing the faster and slower current fluctuations. (e) Histogram plot of the three sections of the RTN in (a) showing the spread of the current levels. (f, g) Plot of the distribution of τ_c and τ_e for the three sections showing that the distributions for Sections 1 and 3 coincide, whereas Section 2 is significantly different.

combination of a slower and a faster current transition, and both transitions appear in an alternate fashion. A zoom-in view of these two trends is plotted in Figures 4b,c. As above, we can understand the signal by dividing into sections and using FHMM analysis. We divide the RTN signal of Figure 4a into six sections based on visual inspection by checking whether the portion of the signal corresponds to the slower or faster current fluctuation. Three of the sections, labeled Section 1 (0−9.31 s), Section 3 (9.35−13.80 s), and Section 5 (14.10−18.40 s) correspond to slower current transitions, while Section 2 (9.31−9.35 s), Section 4 (13.80−14.10 s), and Section 6 (18.40−18.80 s) are faster transitions. Each of these six sections is analyzed using FHMM, and the distributions of τ_c and τ_e for each section are plotted in Figure 4d,e, respectively. Analysis confirms that the distributions of τ_c and τ_e for each of the slower (i.e., Sections 1, 3, and 5) and faster (i.e., Sections 2, 4, and 6) RTN transitions are similar. It is also interesting to note that $\overline{\tau}_C$ and $\overline{\tau}_E$ for slower transitions is almost an order of magnitude higher compared with faster transitions, as shown in Table S3.

The histogram of the RTN data shown in Figure 4a is plotted in Figure 4f and shows at least four distinct current levels. Typically, one would explain this observation by associating the number of current levels with the number of defects (e.g., in this case, four current levels would imply that two distinct defects are modulating the charge transport). However, given that the ΔI for both faster and slower transitions are similar (within statistical uncertainty), it is unlikely that two independent defects are involved here. Rather, an alternative mechanism is simply that a single defect may be perturbed by capture/emission processes at nearby defects or, in general, by some reversible charge rearrangement.

A different example of mutant RTN is shown in Figure 5a in which the amplitude ΔI remains roughly the same for the signal, but there is a sudden change in the time constants between 21−27 s. The complete RTN spectrum collected is provided in Figure S5. On the basis of the visual inspection of the changes in the RTN patterns, the RTN spectrum is separated into three subsections − Section 1 (0−21 s), Section 2 (21−27 s), and Section 3 (27−30 s), and each of the sections is analyzed using FHMM. A zoom-in view of a portion of each section, along with the corresponding FHMM fits, is plotted in Figure 5b−d. Histograms of these three RTN sections are plotted in Figure 5e, showing that the current

https://doi.org/10.1021/acsaelm.2c00559
ACS Appl. Electron. Mater. 2022, 4, 3909−3921

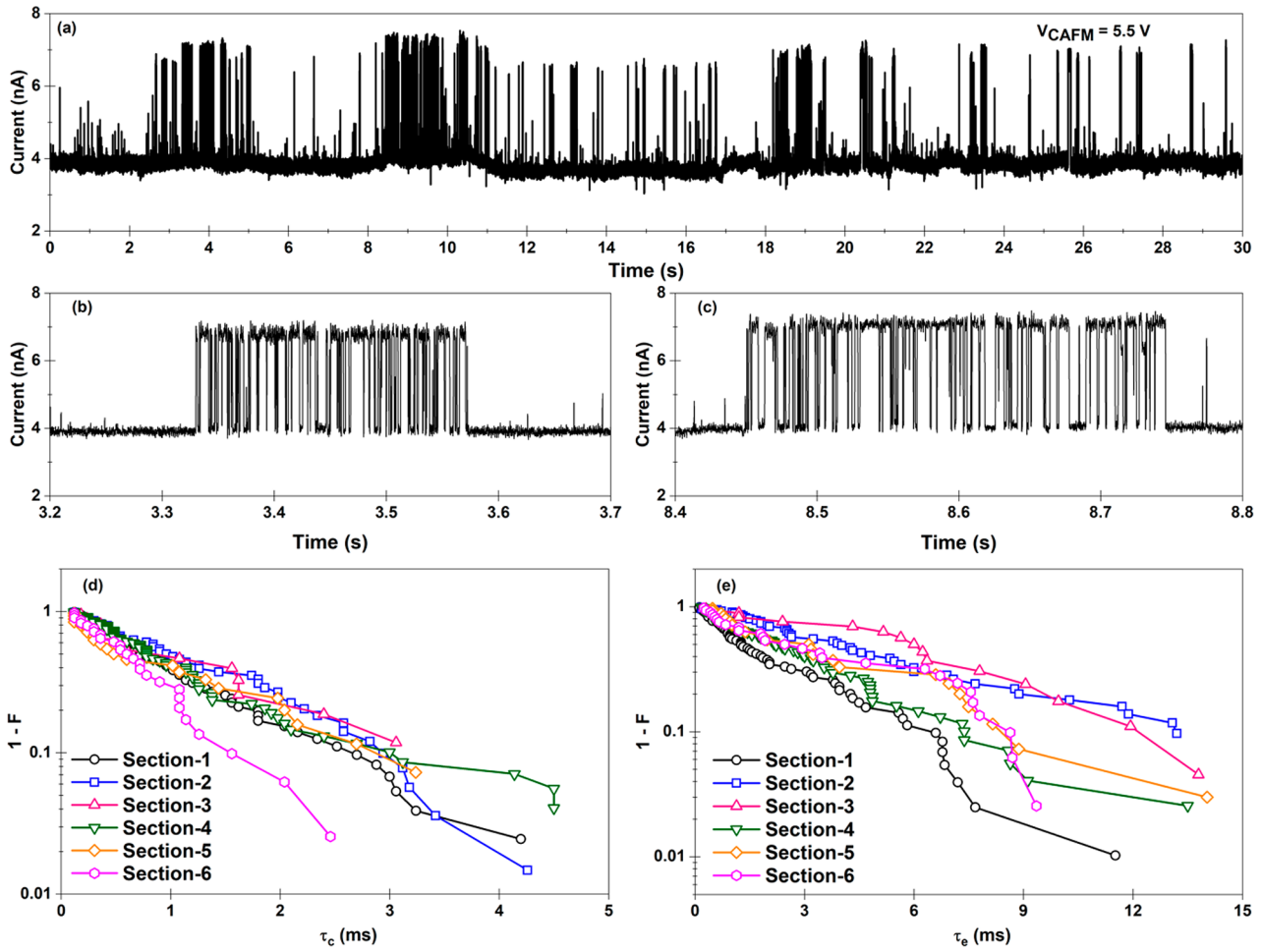

Figure 6. Temporary RTN and analysis: (a) RTN spectra measured after SBD at a bias of 5.5 V at a randomly probed test location. The spectrum shows occurrence of intermittent RTN current fluctuations. (b, c) Zoom-in view of two representative sections of the RTN data in (a) showing the intermittent current fluctuations are essentially two-level RTN. A total of six sections of such two-level RTN are randomly selected and analyzed using FHMM. (d, e) Plot of the distribution of τ_c and τ_e for the six sections showing that, to first order approximation, the RTN features in the six sections are the same and thus identify the same defect.

transitions for the three sections do not overlap completely and the current levels for both low and high states are broad. The extracted values of τ_c and τ_e for the three sections are plotted in Figures 5f, g, respectively. Note that each of the three sections consist of at least 40K (K = 1000) samples which gives an average estimation accuracy of ±12% for the capture and emission times.[43] Hence, the extracted values of $\overline{\tau}_C$ and $\overline{\tau}_E$ for Section 1 and Section 3, shown in Table S4, are comparable within statistical uncertainty, suggesting that the same defect configuration is responsible for the RTN features in Section 1 and Section 3.

2.4.2. Temporary RTN. Figure 6a shows an example of temporary RTN, with the RTN fluctuations only observed at intermittent intervals. In this example, the current remains in the lower current level for the majority of the time with occasional bursts of two-level current fluctuations throughout the entire RTN spectrum, as highlighted in the zoomed-in views plotted in Figures 6b,c. Clearly, in this case, the local charge perturbation in the vicinity of the RTN-inducing defect, although reversible, is strong enough to usually suppress the RTN. We randomly choose six sections from the RTN spectrum in Figure 6a, where consistent two-level RTN fluctuations are present, and analyze these using FHMM. The extracted values of τ_c and τ_e for the six sections are plotted in Figures 6d,e, respectively, and their averaged values are summarized in Table S5. Each of the six sections is composed of only 2−5K samples which leads to an average error of nearly ±30% for capture and emission times. Hence, all the six sections have similar $\overline{\tau}_C$ and $\overline{\tau}_E$ values within error, suggesting that the same defect and electrostatic environment configuration is responsible for all the intermittent bursts of two-level RTN.

2.5. Discussion. *2.5.1. Mechanism of RTN.* Previous studies, reviewed by Li et al.,[44] compare RTN signals generated in many different types of material stacks for application in TRNG. With regards to HfO_2, MIM stacks consisting of Ni/5 nm HfO_2/Au and Au/5 nm HfO_2/Au were found to be rather poor candidates for RTN generating devices because although RTN is observed after SBD (no RTN is observed on fresh devices), the RTN characteristic is slow and of high current. This contrasts with the data shown here for Au-NC HfO_2 showing fast, low current RTN. Clearly, the key question to address is why the presence of nanocrystals changes the RTN response. There is no direct explanation found in the literature and we consider two possible RTN mechanisms, namely a) Coulomb interactions only occur between HfO_2 defects with the nanocrystals confining the defect generation region via highly localized electric fields during SBD, and b) Coulomb

https://doi.org/10.1021/acsaelm.2c00559
ACS Appl. Electron. Mater. 2022, 4, 3909−3921

interactions between the nanocrystal and nearby defects in the HfO_2. We believe the former mechanism to be the most plausible, as discussed below, although it must be emphasized that detailed numerical studies should be undertaken in future to substantiate this important issue.

a. Localized Defect Generation in HfO_2. This is the most straightforward mechanism, with the RTN arising from interactions between defects in the HfO_2. In this standard view,[16] trapping/detrapping at a defect in the HfO_2, principally a neutral oxygen interstitial (O_i^0), perturbs the potential on a nearby oxygen vacancy (V_O) defect via Coulomb interactions (as shown in the energy-level diagram of Figure 7a). If the V_O defect is a pathway for TAT current flow, the perturbation also modulates the current to give the observed RTN. The new role of embedded Au-NC comes from concentrating the electric field (ξ-field). Finite element modeling[45] shows that the presence of NC in a high-κ layer induces asymmetry in the potential distributions in both lateral and vertical directions,[36,46,47] as shown in Figure 7b for HfO_2. The ξ-field is significantly enhanced in the vertical directions by a factor of ~4−5 in the vicinity of a metal NC. This leads to a much increased defect generation rate in the high-κ layer surrounding the NC under SBD. Moreover, the field preferentially confines the location at which both oxygen vacancy and interstitial defects are created. Specifically, given the enhanced ξ-field surrounding the NC, the probability of defect creation in the bulk of the dielectric is suppressed, and most of the electrically stressed defects are strongly confined either above or below the NC (Figure 7c).

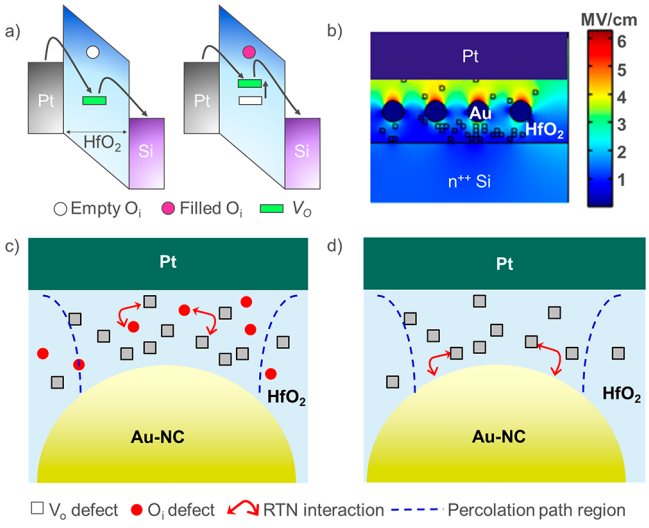

Figure 7. Mechanism of RTN in Au-NC embedded HfO_2: (a) Energy band diagram showing the Coulomb blockade effect leading to RTN in HfO_2. Adapted from Puglisi et al.[16] The charge transfer to the slow O_i defect alters the potential and energy band alignment as shown in the right figure, suppressing the TAT current. The effect is recovered when electron gets emitted from O_i. (b) Kinetic Monte Carlo (KMC) finite element method (FEM) simulation of ξ-field in Au-NC sample. The ξ-field increases by a factor of 4−5 times near the NC, leading to significantly increased defect generation near the Au-NC. Note, for practical reasons, the oxide modeled is relatively thicker than the experimental value, but the qualitative analyses and inferences (enhanced field, localized defect generation) are not affected by this. (c) Schematic showing the scenario in which RTN arises from the electrostatic interaction between positively charged oxygen vacancy (V_O) defects forming the percolation path and nearby neutral oxygen vacancy (O_i) defects. This follows a standard model of RTN as shown in (a) for HfO_2. (d) In this model, RTN arises from interaction between the V_O center(s) forming the percolation path and perturbations of the Coulomb electrostatic field from the charging/discharging of the Au nanocrystal.

The preferential breakdown and defect generation in the HfO_2 above or below the NC has important consequences for RTN. The in-plane dimension of the BD path for the current flow is defined by the NC dimension, and the size of the BD region cannot grow laterally, at least not easily, as the ξ-fields are much higher near the NC. This is significant because current must be injected during the operation of any RTN device, and for standard planar oxides, this may result in the growth of the BD region as more defects are created, which in turn means the RTN could change with time as new defects are created. However, if the BD spot growth is limited by the ξ-fields imposed by the NC, then the RTN will be more stable during operation, especially if the applied voltage is mild, as new defect creation is restricted. This argument has been advanced by Wen et al.[27] for the use of hexagonal boron nitride (h-BN) as a more stable RTN material compared with standard oxides because defect generation cannot propagate easily in the lateral directions of h-BN. We suggest Au-NC embedded HfO_2 also exhibits this attribute.

b. Coulomb Interactions with the Nanocrystal. In this hypothetical mechanism, the trapping defect (i.e., O_i^0) is replaced with the NC. The NC interacts with a V_O defect via Coulomb blockade to create RTN modulations of the TAT current (Figure 7d). The time-dependent change in potential occurs as charge goes on and off the NC. Note that the primary defects to consider remain V_O in the HfO_2 as they carry the TAT current and the diffusion of V_O is low.[48] Also, τ_c and τ_e for trapping on V_O is typically in the ps−ns time scales, and hence, any trapping only contributes to the overall TAT current. Therefore, in this RTN mechanism, the time-dependent RTN fluctuations would be given by the electrostatic charging/discharging of the NC. However, this cannot fully explain the wide variety of nonstationary RTN signals observed in our experiments. Indeed, the Coulomb charging energy[49] for a NC of diameter 4−6 nm in HfO_2 is ~16 meV. Since this is less than the thermal voltage energy (~25 meV), a rather continuous and very fast change in the charge of the NC is expected, which would result in perturbations of the electric field that are not compatible with the discrete and relatively slow nature of the current jumps that are characteristic of the detected RTN signals. This further suggests that the charging and Coulomb blockade effect from the NC is not significant. For this reason, the mechanism (a) above is preferred.

2.5.2. Selected Experimental Observations. We now discuss some of the experimental observations with the understanding that RTN arises from electrostatic interactions between defects within the HfO_2 (i.e., mechanism (a) above).

Both the mutant and temporal RTN (Figures 4, 6) may result from the diffuse motion of oxygen interstitials (O_i), as described by Puglisi et al.[16] Even under the relatively low ξ-field used during RTN measurements, these O_i are mobile and can hop between neighboring interstitial sites. Hence, if an O_i causing RTN drifts in/out of the V_O region, the RTN can change over time because the Coulomb potential modulating the TAT current through the V_O changes. Indeed, if the O_i diffuses entirely out of the Coulomb interaction zone around V_O, the RTN can disappear completely. In HfO_2, the separation between the V_O and O_i defects must be less than

https://doi.org/10.1021/acsaelm.2c00559
ACS Appl. Electron. Mater. 2022, 4, 3909−3921

~1 nm for RTN to manifest itself.[16] Note that trapping at V_O only contributes to the overall TAT current, as mentioned previously. In contrast O_i has much longer τ_c and τ_e (typically between μs and s), and thus, it is the charge trapping at O_i defect sites which dominates the nonstationary RTN. Therefore, all the nonstationary RTN observed are simply manifestations of known phenomena in HfO_2, as also suggested by recent simulation results.[50] With regards to the facile observation of many different RTN signals (two-level, multilevel, mutant, temporal), most generated defects are concentrated in a small BD region above and below the NC (Figures 7b, c). This high defect density in turn leads to many possible electrostatic interactions, giving rise to the various complex and dynamic RTN patterns.

We now consider the BD characteristics (Figures 2a, b). For a bilayer stack consisting only of a low-κ and a high-κ dielectric (e.g., interfacial SiO_2 and HfO_2 in our experiments), in an ideal case the low-κ likely breaks at a lower voltage followed by the high-κ layer,[51] although details depend on the layer permittivity values and thickness. However, the enhanced ξ-field due to metal nanocrystals in the high-κ layer leads to a massive increase in the local defect generation, as shown in Figure 7b, and thus, the defect generation rates in the two dielectric layers may become comparable. This explains the observation in Figure 2a where a majority of the tested locations show an abrupt jump in the current at the onset of breakdown, suggesting that both layers breakdown at the same time after reaching the breakdown field. The test locations which show two discrete jumps in $I-V$ curves (Figure 2b) may point to the separate breakdown of the two dielectric layers, possibly at locations probed by the AFM tip where no nanocrystals were present in the vicinity.

2.5.3. Potential Applications. Recent works have considered the use of RRAM[44] and 2D dielectric materials like h-BN[27] for true random number generation. Our work suggests that metal nanocrystal embedded high-κ stacks could be an alternative. Importantly, NC stacks are already a relatively mature technology used in microelectronics for nonvolatile memory[52−55] and wearable healthcare applications.[56]

Suitable RTN materials and devices for PUF/TRNG require low power, short emission, and capture times, and the RTN signal must be stable and present over longer time frames. Broadly, the Au-NC HfO_2 material satisfies these requirements. We routinely measure continuous two-level RTN signals up to 60 s durations (Figure S3), with the 60 s durations being set by limitations of the experimental setup. This compares favorably with the previous results, indicating suitable RTN properties measured over 20 s timeframes.[27,44]

The need for low power implies the current must be low, both for the RTN and leakage current levels. We typically measure currents on the order of <10 nA at measurement voltages of ~2 V, giving a power of <20 nW. This is a suitably small power dissipation for device application, but some caution is required as one electrode is a sharp AFM tip with a small tip−surface contact area (~50 nm diameter). A realistic microelectronic device would likely have a larger electrode area. Nevertheless, the power loss cannot differ too greatly from the nano-Watt range and preliminary data taken on identical Au-NC HfO_2 film using microfabricated 100 μm diameter capacitor stacks (Figure S6) show RTN after SBD having currents of order ~20 nA.

Short capture and emission times, preferably <100 ms, ensure devices are not too slow for realistic application.[44] In our work, τ_c and τ_e are typically <50 ms (see Figures 4−6 and Tables S1−S5) for two-level RTN signals in Au-NC HfO_2 after SBD, indicating the material has a suitably fast response comparable with reported values.[27,44] Also, the spatial confinement of the defect generation leads to a tighter distribution of the capture/emission time constants, with Lorentzian spectra, which could benefit PUF and TRNG applications. In comparison, the defect generation in HfO_2 (with no NC) is a random Poisson process, resulting in the formation of both correlated and uncorrelated oxygen vacancy and interstitial defects in the bulk of the dielectric. Such spatially distributed defects usually show a wider distribution of the RTN time constants and the effective RTN signals often appear as $1/f$ noise in device level measurements.

Interestingly, the use of NC in a dielectric for inducing local field asymmetry is analogous to the use of the "lightning rod" effect to confine the location of filament formation in another technology platform, namely RRAM devices.[57−60] A consequence of this "lightning rod" effect is the creation of RTN locations over the nanocrystals is self-regulated by the breakdown event itself (i.e., the RTN locations are defined by simply performing SBD on the device). Another attribute of using the Au-NC material is that the voltage necessary to generate defects and induce a SBD is lowered by the presence of the NC.[61]

Not surprisingly for a new platform, there are also detrimental issues which must be considered. The problem of growth of the percolation path over time and resulting variability of the RTN has been discussed above, where we suggest the high ξ-field regions at the top and bottom of the NC confine the percolation path, similar to the lateral confinement mechanism proposed for h-BN.[27] Variability will also be present in the size and distribution of the nanocrystals themselves, which naturally arises in the manufacturing process. However, such variability plays a less prominent role than changes in the dielectric thickness at the top and bottom of the NC (e.g., Figure 1b,c) because the localized ξ-field enhancement dominates the RTN signal generation, the roughness of the metal−dielectric interface, present in any traditional high-κ stack, must be reduced to mitigate such thickness variations. These issues could be greatly reduced in future studies by optimization of the fabrication process.[61] The process flow for metal NC-based stacks is well established[62] for flash storage applications, and this could pave the way for practical applications.

One critical problem which is more difficult to address is variation of the RTN signal over time. Our work shows that the Au-NC material exhibits a DC shift and temporal changes in the time constants of the RTN signal. Therefore, the device and circuit design must be robust to account for such nonidealities to fully exploit RTN for practical TRNG applications. For example, problems of DC level change can be resolved by circuit designs based around high pass filters.[27] Conversely, if the RTN switches off for long periods of time (e.g., Figure 6) this is a significant problem because the circuit simply cannot work if there is no signal.[42] One approach to address such severe temporal RTN changes is to build redundancy into the circuit with several identical stacks running in parallel.

3. CONCLUSIONS

We have demonstrated the application of CAFM for defect nanospectroscopy in ultrathin HfO_2/SiO_2 bilayer dielectrics

https://doi.org/10.1021/acsaelm.2c00559
ACS Appl. Electron. Mater. 2022, 4, 3909−3921

embedded with Au nanocrystals. Combining CAFM defect spectroscopy and FHMM analysis, we analyze RTN after soft breakdown (SBD) and signatures of both two-level and multilevel RTN patterns are observed. Also, the many dynamic electrostatic interactions between defects also provides a unique platform to study nonstationary RTN trends, including mutant and temporary RTN. Significantly, defects generated by SBD are spatially confined near the nanocrystal and this leads to a material exhibiting RTN characteristics that are beneficial for possible use in applications (e.g., low power, short capture and emission times, long duration RTN signals). Given the established compatibility of metal nanocrystal embedded dielectrics with the CMOS processes,[62] this could potentially open a route to codesign materials and circuits for emerging RTN-based technologies, including PUF and TRNG for security in low power IoT networks and devices. To drive toward such applications, it will be important to correlate NC size and density distribution to observed RTN trends and mitigate nonequilibrium RTN in future works. Metal-NC/HfO_2-metal capacitor structures will also need to be fabricated and assessed as basic building blocks for realistic RTN devices possibly through templated self-assembly techniques as well as the use of *in situ* high-resolution TEM setups to examine in real-time the dynamics of defect generation in the presence and absence of NCs, supported by EDX/electron-energy loss spectroscopy analyses.

4. EXPERIMENTAL SECTION

Au Nanocrystal Embedded HfO_2. Highly doped $n^{++}Si$ substrates (ρ = 2−6 Ω-cm) were cleaned in HF solution to remove any native oxide. Atomic layer deposition (ALD) was used to deposit ∼3 nm HfO_2 using H_2O and Tetrakis(dimethylamino) hafnium (TDMAH) as precursors at 250 °C. This is followed by deposition of ∼1.0−1.5 nm Au film using e-beam evaporation and a further 4 nm HfO_2. The sample is finally annealed at 400 °C for 30 min in N_2 ambient, leading to the agglomeration of Au nanocrystals.

Atomic Force Microscopy. An ultrahigh vacuum (UHV) (working pressure of -2×10^{-10} Torr) RHK AFM is used for all the measurements. AFM measurements are done in contact mode, typically at an applied force of 10−40 nN, using all Pt wire cantilevers (Model: RMN12Pt300B, spring constant 0.8 N/m). The tips are cleaned *in situ* in the UHV AFM for 3−5 min using Ar ion milling (Vacuum Microengineering IPS3-D with ion gun IG70) at 5×10^{-6} Torr, 1.2 keV, and 10^{-5} A/cm^2. Note that the use of wire cantilevers also greatly minimizes the effects of tip drift during electrical measurements. In our previous work,[25] we show that soft Pt wire cantilevers can remain over a single breakdown location for well over 1000 s.

TEM Sample Preparation and Measurements. The TEM sample is prepared using focused ion beam in a FEI dual-beam Helios 600i system. A 100−200 nm thick Pt layer is first deposited by an electron beam to protect the sample surface. Subsequently, a 5 μm thick sacrificial Pt layer is deposited using ion beam. Ion milling is used to prepare approximately 10 μm long and 50−70 nm wide TEM lamella, and the prepared lamella is attached to a half Cu TEM grid. A low-energy ion milling (4 keV) is used to remove most of the amorphous (ion-implanted) surface layer from the specimen. A Gatan double tilt TEM holder is used to image the sample in a 200 kV spherical aberration corrected FEI Titan microscope. Imaging is performed in a conventional TEM imaging mode under parallel illumination. A 70 μm objective aperture is centered around the direct electron beam to enhance contrast in the acquired images.

■ ASSOCIATED CONTENT

Supporting Information

The Supporting Information is available free of charge at https://pubs.acs.org/doi/10.1021/acsaelm.2c00559.

TEM micrographs, $I-V$ plots, RTN analysis, and notes on finite element method simulations (PDF)

■ AUTHOR INFORMATION

Corresponding Author

Alok Ranjan − *Engineering Product Development, Singapore University of Technology and Design, Singapore 487 372;* orcid.org/0000-0003-4592-1674; Email: alok_ranjan@sutd.edu.sg

Authors

Francesco Maria Puglisi − *DIEF − Università di Modena e Reggio Emilia, Modena 41125, Italy;* orcid.org/0000-0001-6178-2614

Joel Molina-Reyes − *Electronics Department, National Institute of Astrophysics, Optics and Electronics, Puebla 72840, Mexico;* orcid.org/0000-0002-5681-1713

Paolo Pavan − *DIEF − Università di Modena e Reggio Emilia, Modena 41125, Italy*

Sean J. O'Shea − *Institute of Materials Research and Engineering, Agency for Science Technology and Research, Singapore 138 634;* orcid.org/0000-0003-0385-6245

Nagarajan Raghavan − *Engineering Product Development, Singapore University of Technology and Design, Singapore 487 372;* orcid.org/0000-0001-6735-3108

Kin Leong Pey − *Engineering Product Development, Singapore University of Technology and Design, Singapore 487 372;* orcid.org/0000-0002-0066-091X

Complete contact information is available at: https://pubs.acs.org/10.1021/acsaelm.2c00559

Notes

The authors declare no competing financial interest.

■ ACKNOWLEDGMENTS

The authors would like to acknowledge Prof. Hei Wong (Zhejiang University, China) for providing samples and Dr. Feng Xuan (previously at Zhejiang University) for electrical measurements on the capacitor test structures. We would also like to acknowledge Dr. Mei Sen (alumni of our research group at Singapore University of Technology and Design) for providing the codes for the FEM electric field simulations reported in this work.

■ REFERENCES

(1) Tega, N.; Miki, H.; Pagette, F.; Frank, D. J.; Ray, A.; Rooks, M. J.; Haensch, W., Torii, K. Increasing threshold voltage variation due to random telegraph noise in FETs as gate lengths scale to 20 nm. *2009 Symposium on VLSI Technology* 2009, pp 50−51.

(2) Simoen, E.; Kaczer, B.; Toledano-Luque, M.; Claeys, C. Random Telegraph Noise: From a Device Physicist's Dream to a Designer's Nightmare. *Microelectronics Technology and Devices* **2011**, *39*, 3−15.

(3) Raghavan, N.; Degraeve, R.; Goux, L.; Fantini, A.; Wouters, D. J.; Groeseneken, G.; Jurczak, M. RTN insight to filamentary instability and disturb immunity in ultra-low power switching HfOx and AlOx RRAM. *2013 Symposium on VLSI Technology* 2013, pp T164−T165.

(4) Soni, R.; Meuffels, P.; Petraru, A.; Weides, M.; Kügeler, C.; Waser, R.; Kohlstedt, H. Probing Cu doped Ge0.3Se0.7 based

resistance switching memory devices with random telegraph noise. *J. Appl. Phys.* **2010**, *107*, 024517.
(5) Zhao, M.; Gao, B.; Tang, J.; Qian, H.; Wu, H. Reliability of analog resistive switching memory for neuromorphic computing. *Applied Physics Reviews* **2020**, *7*, 011301.
(6) Suh, G. E.; Devadas, S. Physical Unclonable Functions for Device Authentication and Secret Key Generation. *2007 44th ACM/IEEE Design Automation Conference* 2007, pp 9−14.
(7) Mohanty, A.; Sutaria, K. B.; Awano, H.; Sato, T.; Cao, Y. RTN in Scaled Transistors for On-Chip Random Seed Generation. *IEEE Transactions on Very Large Scale Integration (VLSI) Systems* **2017**, *25*, 2248−2257.
(8) Brown, J.; Gao, R.; Ji, Z.; Chen, J.; Wu, J.; Zhang, J.; Zhou, B.; Shi, Q.; Crowford, J., Zhang, W. A low-power and high-speed True Random Number Generator using generated RTN. *2018 IEEE Symposium on VLSI Technology* 2018, pp 95−96..
(9) Li, X.; Tung, C. H.; Pey, K. L.; Lo, V. L. The physical origin of random telegraph noise after dielectric breakdown. *Appl. Phys. Lett.* **2009**, *94*, 132904.
(10) Grasser, T. Stochastic charge trapping in oxides: From random telegraph noise to bias temperature instabilities. *Microelectronics Reliability* **2012**, *52*, 39−70.
(11) Foster, A. S.; Lopez Gejo, F.; Shluger, A. L.; Nieminen, R. M. Vacancy and interstitial defects in hafnia. *Phys. Rev. B* **2002**, *65*, 174117.
(12) Samuel, R. B.; Gennadi, B.; Alexander, L. S. Modelling of oxygen vacancy aggregates in monoclinic HfO 2: can they contribute to conductive filament formation? *J. Phys.: Condens. Matter* **2015**, *27*, 415401.
(13) Wang, R.; Guo, S.; Zhang, Z.; Zou, J.; Mao, D., Huang, R., Complex Random Telegraph Noise (RTN): What Do We Understand? *2018 IEEE International Symposium on the Physical and Failure Analysis of Integrated Circuits (IPFA)* 2018, pp 1−7..
(14) Vandelli, L.; Padovani, A.; Larcher, L.; Southwick, R. G.; Knowlton, W. B.; Bersuker, G. A Physical Model of the Temperature Dependence of the Current Through SiO2/HfO2 Stacks. *IEEE Trans. Electron Devices* **2011**, *58*, 2878−2887.
(15) Puglisi, F. M.; Pavan, P.; Vandelli, L.; Padovani, A.; Bertocchi, M., Larcher, L. A microscopic physical description of RTN current fluctuations in HfOx RRAM.*2015 IEEE International Reliability Physics Symposium* 2015, pp 5B.5.1−5B.5.6..
(16) Puglisi, F. M.; Larcher, L.; Padovani, A.; Pavan, P. Anomalous random telegraph noise and temporary phenomena in resistive random access memory. *Solid-State Electron.* **2016**, *125*, 204−213.
(17) Gusmeroli, R.; Compagnoni, C. M.; Riva, A.; Spinelli, A. S.; Lacaita, A. L.; Bonanomi, M., Visconti, A., Defects spectroscopy in SiO2 by statistical random telegraph noise analysis, *2006 International Electron Devices Meeting* , pp 1−4..
(18) Trabelsi, M.; Militaru, L.; Sghaier, N.; Souifi, A.; Yacoubi, N. ″Traps centers impact on Silicon nanocrystal memories given by Random Telegraph Signal and low frequency noise″. *Solid-State Electron.* **2011**, *56*, 1−7.
(19) Gehring, A.; Selberherr, S. Modeling of tunneling current and gate dielectric reliability for nonvolatile memory devices. *IEEE Transactions on Device and Materials Reliability* **2004**, *4*, 306−319.
(20) Thamankar, R.; Puglisi, F. M.; Ranjan, A.; Raghavan, N.; Shubhakar, K.; Molina, J.; Larcher, L.; Padovani, A.; Pavan, P.; O'Shea, S. J.; Pey, K. L. Localized characterization of charge transport and random telegraph noise at the nanoscale in HfO2 films combining scanning tunneling microscopy and multi-scale simulations. *J. Appl. Phys.* **2017**, *122*, 024301.
(21) Ranjan, A.; Shubhakar, K.; Raghavan, N.; Thamankar, R.; Bosman, M.; O'Shea, S. J.; Pey, K. L. Localized Random Telegraphic Noise Study in HfO2 dielectric stacks using Scanning Tunneling Microscopy - Analysis of process and stress-induced traps. *Proceedings of the International Symposium on the Physical and Failure Analysis of Integrated Circuits, IPFA* 2015. DOI: 10.1109/IPFA.2015.7224356.
(22) Welland, M. E.; Koch, R. H. Spatial location of electron trapping defects on silicon by scanning tunneling microscopy. *Appl. Phys. Lett.* **1986**, *48*, 724−726.
(23) Ranjan, A.; Raghavan, N.; Shubhakar, K.; O'Shea, S. J.; Pey, K. L. Random Telegraph Noise Nano-Spectroscopy in High-κ Dielectrics Using Scanning Probe Microscopy Techniques. In *Noise in Nanoscale Semiconductor Devices*; Grasser, T., Ed.; Springer International Publishing, 2020; pp 417−440.
(24) Ranjan, A.; Puglisi, F. M.; Raghavan, N.; O'Shea, S. J.; Shubhakar, K.; Pavan, P.; Padovani, A.; Larcher, L.; Pey, K. L. Random Telegraph Noise in 2D Hexagonal Boron Nitride Dielectric Films. *Appl. Phys. Lett.* **2018**, *112*, 133505.
(25) Ranjan, A.; Pey, K. L.; O'Shea, S. J. The interplay between drift and electrical measurement in conduction atomic force microscopy. *Rev. Sci. Instrum.* **2019**, *90*, 073701.
(26) Ranjan, A. Nanoscale Noise Spectroscopy and Breakdown Studies in Hafnium Dioxide and 2D Hexagonal Boron Nitride Dielectrics. Ph.D. Thesis, Engineering Product Development, Singapore University of Technology and Design, 2019.
(27) Wen, C.; Li, X.; Zanotti, T.; Puglisi, F. M.; Shi, Y.; Saiz, F.; Antidormi, A.; Roche, S.; Zheng, W.; Liang, X.; Hu, J.; Duhm, S.; Roldan, J. B.; Wu, T.; Chen, V.; Pop, E.; Garrido, B.; Zhu, K.; Hui, F.; Lanza, M. Advanced Data Encryption using 2D Materials. *Adv. Mater.* **2021**, *33*, 2100185.
(28) Brown, J.; Zhang, J. F.; Zhou, B.; Mehedi, M.; Freitas, P.; Marsland, J.; Ji, Z. Random-telegraph-noise-enabled true random number generator for hardware security. *Sci. Rep.* **2020**, *10*, 17210.
(29) Chungho Lee; Ganguly, U.; Narayanan, V.; Tuo-Hung Hou; Jinsook Kim; Kan, E.C. Asymmetric electric field enhancement in nanocrystal memories. *Ieee Electron Device Letters* **2005**, *26*, 879−881.
(30) Puglisi, F. M.; Pavan, P. RTN analysis with FHMM as a tool for multi-trap characterization in HfOX RRAM *2013 IEEE International Conference of Electron Devices and Solid-state Circuits* 2013, pp 1−2.
(31) Wu, X.; Migas, D. B.; Li, X.; Bosman, M.; Raghavan, N.; Borisenko, V. E.; Pey, K. L. Role of oxygen vacancies in HfO2-based gate stack breakdown. *Appl. Phys. Lett.* **2010**, *96*, 172901.
(32) Gao, D. Z.; Strand, J.; El-Sayed, A.; Shluger, A. L.; Padovani, A., Larcher, L., Role of electron and hole trapping in the degradation and breakdown of SiO_2 and HfO_2 films. *2018 IEEE International Reliability Physics Symposium (IRPS)* 2018, pp 5A.2-1−5A.2-7..
(33) Ranjan, A.; O'Shea, S. J.; Bosman, M.; Molina, J.; Raghavan, N., Pey, K. L. Correlation of dielectric breakdown and nanoscale adhesion in silicon dioxide thin films. *2020 IEEE International Reliability Physics Symposium (IRPS)* 2020, pp 1−7..
(34) Wu, E. Y.; Li, B.; Stathis, J. H. Modeling of time-dependent non-uniform dielectric breakdown using a clustering statistical approach. *Appl. Phys. Lett.* **2013**, *103*, 152907.
(35) Wu, E.; Stathis, J.; Li, B.; Linder, B.; Zhao, K.; Bonilla, G. A critical analysis of sampling-based reconstruction methodology for dielectric breakdown systems (BEOL/MOL/FEOL) *2015 IEEE International Reliability Physics Symposium* 2015, pp 2A.2.1−2A.2.11..
(36) Lee, C.; Ganguly, U.; Narayanan, V.; Hou, T.-H.; Kim, J.; Kan, E. C. Asymmetric electric field enhancement in nanocrystal memories. *IEEE Electron Device Lett.* **2005**, *26*, 879−881.
(37) Acal, C.; Ruiz-Castro, J. E.; Aguilera, A. M.; Jiménez-Molinos, F.; Roldán, J. B. Phase-type distributions for studying variability in resistive memories. *Journal of Computational and Applied Mathematics* **2019**, *345*, 23−32.
(38) Ruiz-Castro, J. E.; Acal, C.; Aguilera, A. M.; Roldán, J. B. A Complex Model via Phase-Type Distributions to Study Random Telegraph Noise in Resistive Memories. *Mathematics* **2021**, *9*, 390.
(39) Ranjan, A.; Raghavan, N.; Shubhakar, K.; Thamankar, R.; Molina, J.; Shea, S. J. O.; Bosman, M.; Pey, K. L. CAFM based spectroscopy of stress-induced defects in HfO2 with experimental evidence of the clustering model and metastable vacancy defect state. *2016 IEEE International Reliability Physics Symposium (IRPS)* 2016, pp 7A-4-1−7A-4-7..
(40) Kalantarian, A.; Bersuker, G.; Gilmer, D. C.; Veksler, D.; Butcher, B.; Padovani, A.; Pirrotta, O.; Larcher, L.; Geer, R.; Nishi, Y.;

Kirsch, P. Controlling uniformity of RRAM characteristics through the forming process. *2012 IEEE International Reliability Physics Symposium (IRPS)* 2012, 6C.4.1−6C.4.5.
(41) Puglisi, F. M.; Pavan, P.; Padovani, A.; Larcher, L.; Bersuker, G. Random Telegraph Signal noise properties of HfOx RRAM in high resistive state. *2012 Proceedings of the European Solid-State Device Research Conference (ESSDERC)* 2012, pp 274−277.
(42) Guo, S.; Wang, R.; Mao, D.; Wang, Y.; Huang, R. Anomalous random telegraph noise in nanoscale transistors as direct evidence of two metastable states of oxide traps. *Sci. Rep.* **2017**, *7*, 6239.
(43) Puglisi, F. M.; Pavan, P. Guidelines for a Reliable Analysis of Random Telegraph Noise in Electronic Devices. *IEEE Transactions on Instrumentation and Measurement* **2016**, *65*, 1435−1442.
(44) Li, X.; Zanotti, T.; Wang, T.; Zhu, K.; Puglisi, F. M.; Lanza, M. Random Telegraph Noise in Metal-Oxide Memristors for True Random Number Generators: A Materials Study. *Adv. Funct. Mater.* **2021**, *31*, 2102172.
(45) Mei, S.; Raghavan, N.; Bosman, M.; Linten, D.; Groeseneken, G.; Horiguchi, N.; Pey, K. L. New understanding of dielectric breakdown in advanced FinFET devices — physical, electrical, statistical and multiphysics study *2016 IEEE International Electron Devices Meeting (IEDM)* **2016**, pp 15.5.1−15.5.4..
(46) Hou, T. H.; Lee, C.; Narayanan, V.; Ganguly, U.; Kan, E. C. Design Optimization of Metal Nanocrystal Memory - Part I: Nanocrystal Array Engineering. *IEEE Trans. Electron Devices* **2006**, *53*, 3095−3102.
(47) Hou, T. H.; Lee, C.; Narayanan, V.; Ganguly, U.; Kan, E. C. Design Optimization of Metal Nanocrystal Memory-Part II: Gate-Stack Engineering. *IEEE Trans. Electron Devices* **2006**, *53*, 3103−3109.
(48) Foster, A. S.; Shluger, A. L.; Nieminen, R. M. Mechanism of Interstitial Oxygen Diffusion in Hafnia. *Phys. Rev. Lett.* **2002**, *89*, 225901.
(49) Beenakker, C. W. J. Theory of Coulomb-blockade oscillations in the conductance of a quantum dot. *Phys. Rev. B* **1991**, *44*, 1646−1656.
(50) Vecchi, S.; Pavan, P.; Puglisi, F. M. The Relevance of Trapped Charge for Leakage and Random Telegraph Noise Phenomena. *IEEE International Reliability Physics Symposium* 2022, pp 1−6..
(51) Padovani, A.; Raghavan, N.; Larcher, L.; Pey, K. L. Identifying the First Layer to Fail in Dual-Layer SiOX/HfSiON Gate Dielectric Stacks. *IEEE Electron Device Lett.* **2013**, *34*, 1289−1291.
(52) Tiwari, S.; Rana, F.; Hanafi, H.; Hartstein, A.; Crabbé, E. F.; Chan, K. A silicon nanocrystals based memory. *Appl. Phys. Lett.* **1996**, *68*, 1377−1379.
(53) Tan, Z.; Samanta, S. K.; Yoo, W. J.; Lee, S. Self-assembly of Ni nanocrystals on HfO2 and N-assisted Ni confinement for nonvolatile memory application. *Appl. Phys. Lett.* **2005**, *86*, 013107.
(54) Kim, H.; Woo, S.; Kim, H.; Bang, S.; Kim, Y.; Choi, D.; Jeon, H. Pt Nanocrystals Embedded in Remote Plasma Atomic-Layer-Deposited HfO2 for Nonvolatile Memory Devices. *Electrochem. Solid-State Lett.* **2009**, *12*, H92.
(55) Yang, F. M.; Chang, T. C.; Liu, P.-T.; Yeh, Y. H.; Yu, Y. C.; Lin, J. Y.; Sze, S. M.; Lou, J. C. Nickel silicide nanocrystals embedded in SiO2 and HfO2 for nonvolatile memory application. *Thin Solid Films* **2007**, *516*, 360−363.
(56) Kim, J.; Son, D.; Lee, M.; Song, C.; Song, J.-K.; Koo, J. H.; Lee, D. J.; Shim, H. J.; Kim, J. H.; Lee, M.; Hyeon, T.; Kim, D.-H. A wearable multiplexed silicon nonvolatile memory array using nanocrystal charge confinement. *Science Advances* **2016**, *2*, No. e1501101.
(57) Park, J.; Jo, M.; Lee, J.; Jung, S.; Kim, S.; Lee, W.; Shin, J.; Hwang, H. Improved Switching Uniformity and Speed in Filament-Type RRAM Using Lightning Rod Effect. *IEEE Electron Device Lett.* **2011**, *32*, 63−65.
(58) Liu, Q.; Long, S.; Wang, W.; Tanachutiwat, S.; Li, Y.; Wang, Q.; Zhang, M.; Huo, Z.; Chen, J.; Liu, M. Low-Power and Highly Uniform Switching in ZrO2-Based ReRAM With a Cu Nanocrystal Insertion Layer. *IEEE Electron Device Lett.* **2010**, *31*, 1299−1301.
(59) Lee, D.; Song, J.; Woo, J.; Park, J.; Park, S.; Cha, E.; Lee, S.; Koo, Y.; Moon, K.; Hwang, H. Optimized Lightning-Rod Effect to Overcome Trade-Off Between Switching Uniformity and On/Off Ratio in ReRAM. *IEEE Electron Device Lett.* **2014**, *35*, 214−216.
(60) Wu, Q.; Banerjee, W.; Cao, J.; Ji, Z.; Li, L.; Liu, M. Improvement of durability and switching speed by incorporating nanocrystals in the HfOx based resistive random access memory devices. *Appl. Phys. Lett.* **2018**, *113*, 023105.
(61) Kumar, K. V.; Goud, J. P.; Kumar, K. R.; Raju, K. C. J.; Rao, S. V. S. N. Laser annealing of Au/HfO2 bi-layers to fabricate Au nanoparticles without altering the phase of HfO2 for applications in SERS and memory devices. *Journal of Materials Science: Materials in Electronics* **2022**, *33*, 6657−6669.
(62) Liu, Z.; Lee, C.; Narayanan, V.; Pei, G.; Kan, E. C. Metal nanocrystal memories. I. Device design and fabrication. *IEEE Trans. Electron Devices* **2002**, *49*, 1606−1613.

https://doi.org/10.1021/acsaelm.2c00559
ACS Appl. Electron. Mater. 2022, 4, 3909−3921